Dynamics of a sheared twist-bend nematic liquid crystal

M. Praveen Kumar [1], Jakub Karcz [2], Przemyslaw Kula,[2] and Surajit Dhara [1,*]

[1]*School of Physics, University of Hyderabad, Hyderabad-500046, India*

[2]*Institute of Chemistry, Faculty of Advanced Technologies and Chemistry, Military University of Technology, 00-908 Warsaw, Poland*

We study the flow behavior of a twist-bend nematic (N_{TB}) liquid crystal. It shows three dynamic regimes in certain temperature and shear-rate range. In region I, $\sigma \sim \sqrt{\dot{\gamma}}$, in region II, the stress shows a near plateau, characterized by a power law $\sigma \sim \dot{\gamma}^\alpha$, where $\alpha \sim 0.1$–0.4 and in region III, $\sigma \sim \dot{\gamma}$. With increasing shear rate, σ changes continuously from region I to II, whereas it changes discontinuously with a hysteresis from region II to III. In the near plateau (region II), we observe dynamic stress fluctuations, exhibiting regular, periodic, and quasiperiodic oscillations under the application of a steady shear. The observed spatiotemporal dynamics are close to those predicted theoretically in sheared nematogenic fluids.

I. INTRODUCTION

Structure and flow behavior of complex fluids such as colloidal suspensions, polymeric systems, surfactant gels, and liquid crystals have been a subject of increasing interests [1–4]. These soft materials exhibit strong response under a moderate or weak external perturbation. Among them, liquid crystals (LCs) exhibit mesomorphic properties, i.e., variety of thermodynamically stable phases. Some commonly occurring phases in thermotropic LCs are nematic, smectic, and cholesteric [5,6]. Nematic phase has only the orientational order, smectic has additionally a lamellar structure, and in cholesteric the director (average orientation direction of the molecules) forms a helical structure. Because of the weak intermolecular interactions, the structure of LCs can be easily deformed by external forces such as electric, magnetic [7], and stress field [8–14]. In fact the optical response of nematic LCs due to the electric field has been exploited in the liquid crystal display (LCDs) applications. The applied stress field not only changes the orientation and equilibrium structure but also changes the flow behavior of the LCs which are mostly unknown for many new LCs discovered lately.

In the recent past, a new nematic phase, called the twist-bend nematic (N_{TB}), made of achiral molecules has been discovered, in which the director forms an oblique helicoid ($0 < \theta < \pi/2$) with a nanoscale periodicity [Fig. 1(a)] [15–23]. The structure of N_{TB} phase is very different than that of the cholesteric LCs made of chiral molecules, where $\theta = \pi/2$ and the pitch of the helix is much larger (a few hundred nm) [6]. The heliconical pitch of N_{TB} is of the order of a few molecular length and can be regarded as "pseudolayers" without a true mass density wave, unlike smectics [24]. Interestingly, the pseudolayers of the N_{TB} LCs exhibit compression elastic modulus, similar to the conventional smectics but with an order of magnitude lower value [25,26]. It is interesting to investigate and understand from the fundamental perspective how the novel nematic phase responds to the applied stress field. Is the flow behavior of N_{TB} LCs, nematiclike or smecticlike? To address these questions, we systematically investigated the flow behavior of a N_{TB} LC. We show that the studied N_{TB} LC exhibits three dynamic regimes in the $\dot{\gamma} - T$ diagram. In the intermediate regime it shows time dependent stress oscillations, which proceeds from periodic to aperiodic state with increasing temperature.

II. EXPERIMENT

We have synthesized a dimeric liquid crystal, α, ω-bis(4,4-'cyanobiphenyl nonane), which is known as CB9CB in short. A summary of the synthesis scheme is presented in Appendix B. Two cyanobiphenyl units are connected through nine ($n = 9$) flexible methylene units [Fig. 1(b)]. The phase transitions and textures were observed using a polarizing optical microscope (Olympus BX51) and a temperature controller (Mettler FP 90). In cooling, it exhibits the following phase transitions: I → N 124 °C, N → N_{TB} 108 °C, N_{TB} → Cr 84 °C. These transition temperatures are comparable to those reported by Paterson *et al.* [27]. Polarizing optical microscope textures in planar and in homeotropic cells are shown in Fig. 1(c). The textures of N_{TB} phase are very different than the usual nematics and somewhat similar to those of the focal conic textures of SmA LCs. We have used a strain controlled Rheometer (MCR 501, Anton Paar) with a cone-plate measuring system having plate diameter of 25 mm and the cone angle of 1° for all rheological measurements. A Peltier temperature controller was attached with the bottom plate for controlling the temperature with an accuracy of 0.1 °C. A hood was used to cover the measuring system for maintaining uniformity of the sample temperature. A fresh sample was mounted for each measurement and it was heated above the nematic-isotropic transition temperature and then cooled at the rate 1 °C/min to the N_{TB} phase. The sample was presheared for five minutes at a low shear rate (5 s^{-1}) before starting the measurements. The phase transition temperatures of the mounted samples in the Rheometer were ascertained from the temperature-dependent viscosity that shows characteristic viscosity change at the phase transitions. The stress

*surajit@uohyd.ac.in
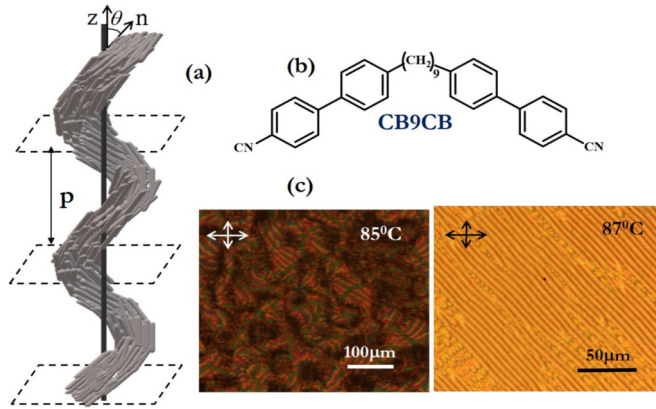
FIG. 1. (a) Schematic view of heliconical orientation of the molecules in the N_{TB} phase. Separation between the two dotted planes represents pitch p, equivalent to the pseudolayer thickness. (b) Chemical structure of the compound CB9CB. (c) Polarizing optical microscope textures in the N_{TB} phase in a homeotropic (left) and in a homogeneous (right) cells.

relaxation data is collected at each second for the duration of 60 minutes.

III. RESULTS AND DISCUSSION

Figure 2(a) shows the flow curves at different temperatures in the N_{TB} phase in log-log scale. The data in the linear scale from the starting shear rate is also presented in Appendix A (Fig. 9). At a fixed temperature, initially the stress (σ) increases with shear rate ($\dot{\gamma}$) and at a particular shear rate ($\dot{\gamma}_L$), the stress changes slope and tends to saturate, showing a near plateau. At a certain higher shear rate ($\dot{\gamma}_U$), the stress jumps discontinuously to a larger value from the near plateau and continues to increase with increasing shear rate. Similar discontinuous transition is also observed with decreasing shear rate. But the transition takes place at a slightly higher shear rate, showing a clear thermal hysteresis [inset to Fig. 2(b)], a typical characteristic of discontinuous transition. At higher temperatures the discontinuous transition takes place at higher shear rates. The variations of the shear rates $\dot{\gamma}_L$ and $\dot{\gamma}_U$ with temperature are shown in Fig. 2(b). We observe three distinct regimes. The transition from region I to region II takes place continuously whereas from region II to region III, the transition takes place discontinuously. Beyond $T \simeq 97\,°C$ the near plateau is not observed although the stress jump is observed until $T \simeq 103\,°C$.

Figure 3(a) shows the variation of stress with the shear rate in region I. It shows a non-Newtonian flow behavior and the data can be fitted to the scaling relation $\sigma \sim C_1(T)\dot{\gamma}^{1/2}$, where $C_1(T)$ is a proportionality constant that varies with temperature. This also means that the shear viscosity decreases as $\eta \sim \dot{\gamma}^{-1/2}$, exhibiting a shear thinning behavior. The constant $C_1(T)$ decreases with increasing temperature and it can be fitted to $C_1(T) \sim (T_c - T)^{0.53\pm0.01}$, where T_c (=103 °C) is the temperature above which the discontinuous transition is not detectable. It is noticed that T_c is about 5 °C below the N to N_{TB} transition temperature (108 °C).

The near plateau has a finite slope and can be fitted to the power law: $\sigma \sim \dot{\gamma}^{\alpha}$ where α is an exponent that increases
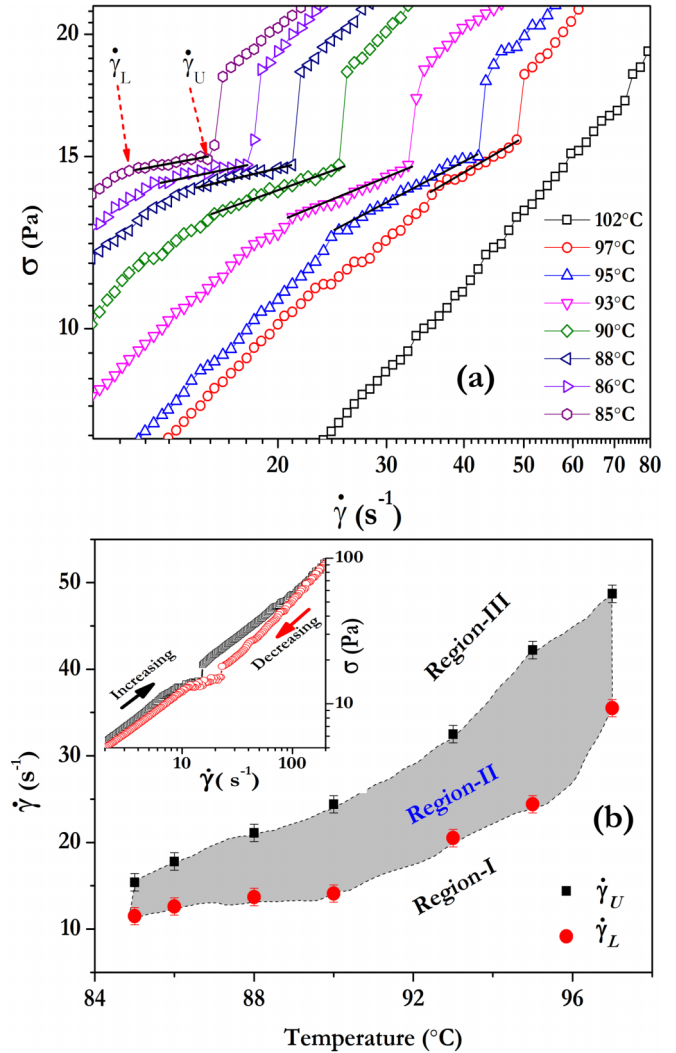
FIG. 2. (a) Flow curves at different temperatures in the N_{TB} phase of CB9CB LC. Solid lines show best fits to $\sigma \sim \dot{\gamma}^{\alpha}$. (b) Temperature variation of the onset shear rate $\dot{\gamma}_L$ (red circles) and the terminal shear rate $\dot{\gamma}_U$ (black squares) of the near plateau. Dotted curve is a guide to the eye. Inset shows the hysteresis of the transition at $T = 85\,°C$. The difference between the two shear rates in heating and cooling at the transition is $\Delta\dot{\gamma} = \dot{\gamma}_U - \dot{\gamma}_L = 8\,s^{-1}$.

linearly with the temperature from 0.1 to 0.4 as shown in Fig. 4(a). Figure 4(b) shows the variation of stress jump $\Delta\sigma$ with temperature. It decreases approximately from 3.5 Pa to 1 Pa as the temperature is increased to $T_c = 102\,°C$. Similar near plateau has been observed in shear-banding micellar aqueous solutions of surfactant [cetyl trimethylammonium tosulate (CTAT)] as a function of salt concentration [28]. It was explained, taking into account the effect of coupling of flow concentration [28–38] and flow microstructures [39]. Ours is a single component thermotropic LC hence the possibility of flow-concentration coupling is ruled out. The stress plateau has also been observed in wormlike micellar systems very near to the nematic to isotropic phase transition, wherein the low (isotropic) and high viscous (nematic) regions are separated, forming shear bands [33]. But in our system, the near plateau is observed below 100 °C which is about 8 °C below the N-N_{TB} phase transition temperature. Hence, the
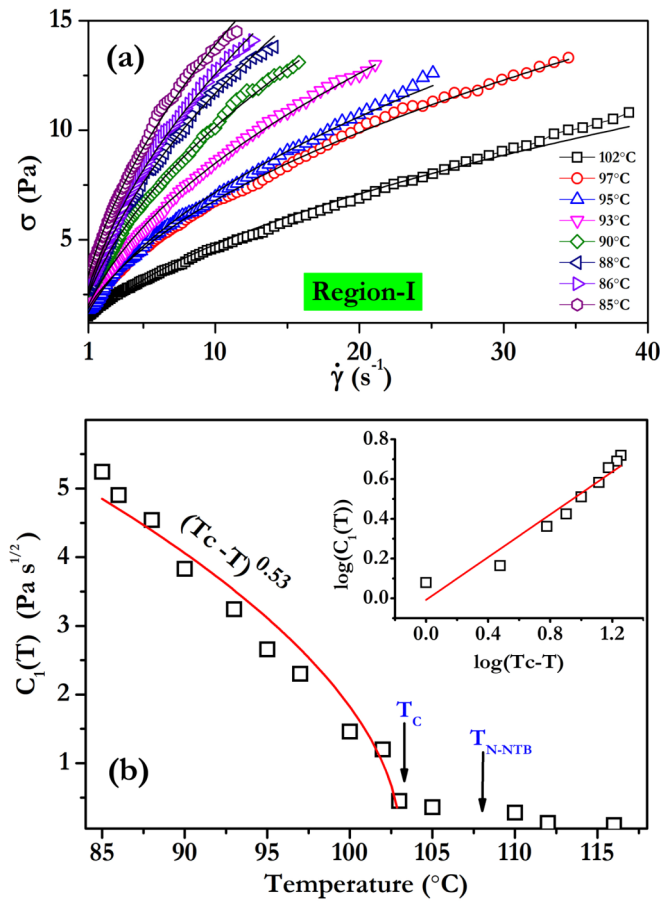
FIG. 3. (a) Variation of σ with $\dot{\gamma}$ in region I at different temperatures in the N_{TB} phase. Solid lines are best fits to $\sigma \sim C_1(T)\sqrt{\dot{\gamma}}$. (b) Temperature variation of slope $C_1(T)$. Solid red curve is a least square fit to $C_1(T) \sim (T_c - T)^{0.53\pm0.01}$ with $T_c = 103°C$. Both temperatures, T_c and nematic to N_{TB} transition ($T_{N\text{-}NTB}$), are marked by vertical arrows. Inset shows a log-log plot.

shear banding or mixing of N and N_{TB} phases can be ruled out.

In region III, the N_{TB} phase shows a Newtonian flow behavior [Fig. 5(a)] and the stress can be fitted to the scaling relation $\sigma \sim C_3(T)\dot{\gamma}$, where $C_3(T)$ is equivalent to the effective viscosity η_{eff}. Figure 5(b) shows that $C_3(T)$ decreases with increasing temperature as expected.

The effect of shear in the SmA phase of 4-cyano-4′-octylbiphenyl (8CB) liquid crystal has been studied using a stress-controlled rheometer, in which the stress was applied and the strain was measured [31]. Interestingly, the shear response of the N_{TB} phase is somewhat similar to that of the SmA phase of 8CB LC, except the regimes in N_{TB} appear at much higher shear rate. From the simultaneous rheo-x-ray investigations of the 8CB LC, two steady state orientations of lamellae were identified in a certain temperature range of the SmA phase. In the low shear-rate regime (equivalent to region I), multilamellar cylinders are formed which are oriented along the flow direction as shown schematically in Fig. 6(a) and the system shows a non-Newtonian flow behavior namely, $\sigma \sim \sqrt{\dot{\gamma}}$, similar to that observed in the present sample. At high shear-rate regime (equivalent to region III), SmA layers are oriented perpendicular to the shear plane as shown in
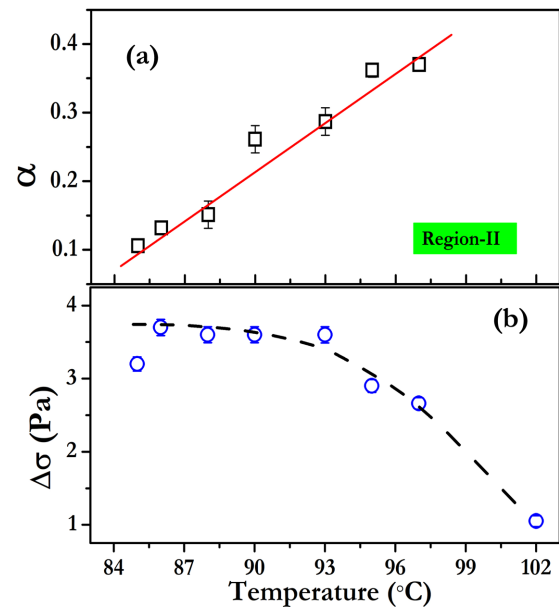
FIG. 4. (a) Temperature variation of α in the near plateau. Solid red line is a best fit to the data. (b) Temperature variation of the stress jump $\Delta\sigma$ in the N_{TB} phase. Dashed curve is drawn as a guide to the eye.

Fig. 6(b) and $\sigma \sim \dot{\gamma}$. In the intermediate shear rate range, a diphasic region was observed where these two states coexist.

The SmA phase of 8CB LC has a layer thickness ~ 2 nm with a mass density wave, whereas the N_{TB} phase of CB9CB LC has a pseudolayer structure (pitch ~ 9 nm) without a true mass density wave [23]. Moreover, the pseudolayers of N_{TB} phase exhibit compression elastic modulus whose value is one to two orders of magnitude lower than that of the SmA phase [26]. Considering the structural similarities between the SmA and N_{TB} phases, it is more likely that in region I of the N_{TB} phase, the pseudolayers form multipseudolamellar cylinders which are oriented along the flow direction and in region III the pseudolayers are oriented perpendicular to the shearing plates as shown schematically in Fig. 6. Region II is a diphasic region wherein the pseudolayers and multipseudolamellar cylinders coexist. At higher temperatures ($>102°C$) and high shear rates (>80 s^{-1}), the N_{TB} phase may completely transit to N phase. However, confirmation of such dynamic features require further rheo-microscopy or rheo-x-ray investigations.

The existence of stress plateau is often a signature of shear-banded inhomogeneous stationary flows resulting mechanical instability [37]. The time-dependent stress in this regime usually shows dynamic relaxation [38,40]. In order to study the stress dynamics in the near-plateau region we have measured the time dependence of stress under a steady shear at a few temperatures. Figure 7(a) shows the time-dependent stress profiles at some selected shear rates, namely $\dot{\gamma} = 5, 10, 12, 15, 18$ s^{-1} and at a fixed temperature ($T = 85°C$) in the N_{TB} phase. Among these shear rates, 5 s^{-1} lies just below and shear rate 18 s^{-1} lies just above the near-plateau regime. The stress values (σ) for these two shear rates (beyond the near-plateau regime) is almost independent of time. When the shear rate is increased to 10 s^{-1}, σ shows oscillation which looks periodic and the patterns change at higher shear rates
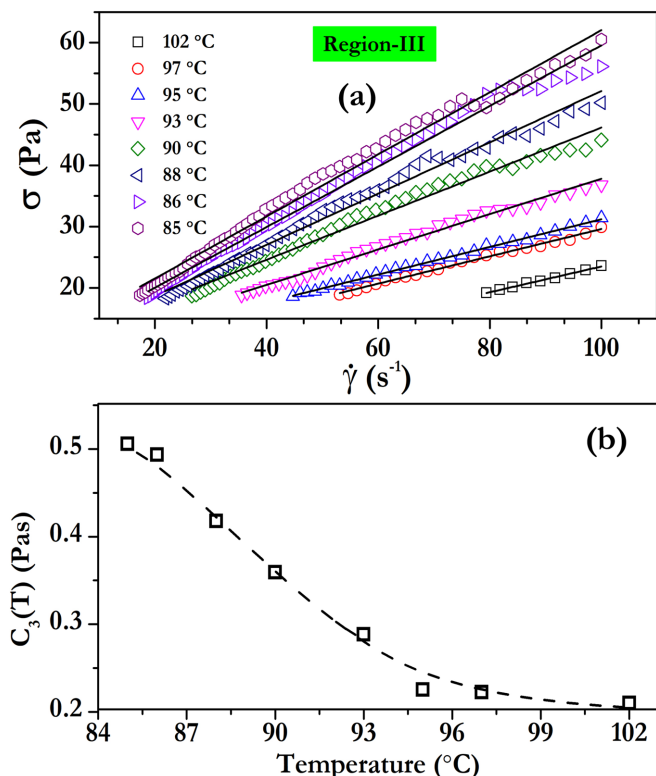
FIG. 5. (a) Variation of stress σ with $\dot{\gamma}$ in region III at different temperatures in the N_{TB} phase. Solid lines are best fits to $\sigma \sim C_3(T)\dot{\gamma}$. (b) Temperature variation of $C_3(T)$. Dashed curve is drawn as a guide to the eye.

($\dot{\gamma} = 12$ and 15 s^{-1}). It may be mentioned that the amplitude of the oscillation is much larger than the limiting stress value of the plate-cone geometry (24 mPa.s^{-1}) therefore, the stress signal is due to the dynamic response of the sample. The Fourier power spectrums of the signals for the shear rates, $\dot{\gamma} = 10, 12$ and 15 s^{-1} are shown in Fig. 7(b). The oscillations at 10 s^{-1} shows a fundamental mode (ω) and its higher harmonics. The frequency ω of the fundamental mode is shifted to higher values with increasing shear rate. For example, the frequencies ($\omega = 2\pi f$) for the fundamental modes for shear rates, $\dot{\gamma} = 10, 12,$ and 15 s^{-1} are 0.17 rad/s, 0.21 rad/s, and 0.27 rad/s, respectively. The driving angular frequency (Ω) of the plate-cone system for a given shear rate $\dot{\gamma}$, is given by $\Omega = \dot{\gamma}\tan(\alpha)$, where α ($=1°$) is the cone angle. The calculated driving frequencies Ω for the shear rates 10, 12, and 15 s^{-1} are 0.17, 0.21, and 0.26 rad/s, respectively, which are almost equal to the respective fundamental frequencies, i.e., $\Omega = \omega$ [Fig. 7(b)]. This suggests that the stress oscillations in the near plateau are driven by the shearing force.
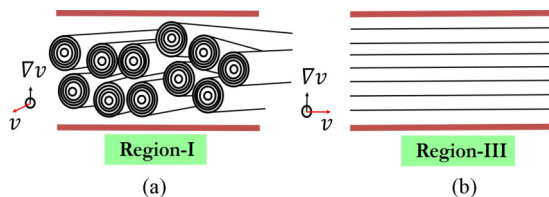
FIG. 6. Schematic diagram showing (a) multipseudolamellar cylinders in region I and (b) parallel pseudolayers in region III.
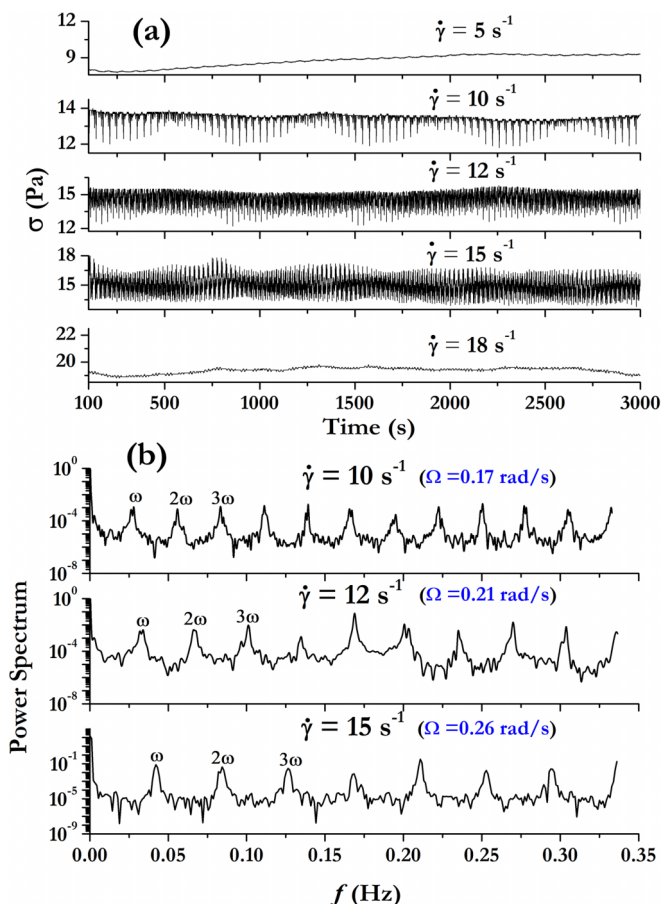
FIG. 7. (a) Stress dynamics in the near-plateau regime at $T = 85°C$. The stress oscillation time series at different shear rates. Shear rates $\dot{\gamma} = 10, 12, 15$ s^{-1} lie within the stress plateau. $\dot{\gamma} = 5$ and 18 s^{-1} lies just below and above the stress plateau, respectively [see Fig. 2(a)]. (b) Corresponding Fourier power spectrum. A few harmonics of the fundamental frequency ω ($= 2\pi f$) are labeled. The fundamental frequencies ω for the shear rates 10,12,15 s^{-1} are 0.17, 0.21, and 0.27 rad/s, respectively. Shearing frequencies calculated using $\Omega = \dot{\gamma}\tan(\alpha)$ are also shown in blue within brackets next to the shear rates.

Figure 8 shows time-dependent stress profile and the corresponding power spectra at a higher temperature ($T = 95°C$). Shear rates 10 and 50 s^{-1} lie below and above the near-plateau regime and the corresponding stress values are almost constant [Fig. 8(a)]. Shear rates 27, 30, and 35 s^{-1} are well within the range of near plateau. The stress signal corresponding to $\dot{\gamma} = 27$ s^{-1} looks periodic with two modes but the power spectrum shows that there is a fundamental frequency ω, which is identified as equal to the shearing frequency Ω and also its higher harmonics, e.g., 2ω, 3ω, and 4ω. Apart from these, there are two more frequencies ω_1, ω_2 and their higher harmonics, and there are also several linear combinations of frequencies such as $\omega + \omega_1$, $\omega + \omega_2$, $\omega_1 + 2\omega$, $2\omega + \omega_2$, $3\omega + \omega_1$, $2\omega - \omega_1$, and $\omega_1 - \omega$ etc. These additional features are the hallmark of quasiperiodic signal. The stress oscillation corresponding to the shear rate 30 s^{-1} apparently looks periodic [Fig. 8(a)]. The stress oscillation at shear rate 35 s^{-1} and the corresponding power spectrum shows that the oscillation is quasiperiodic and apart from the three primary frequencies
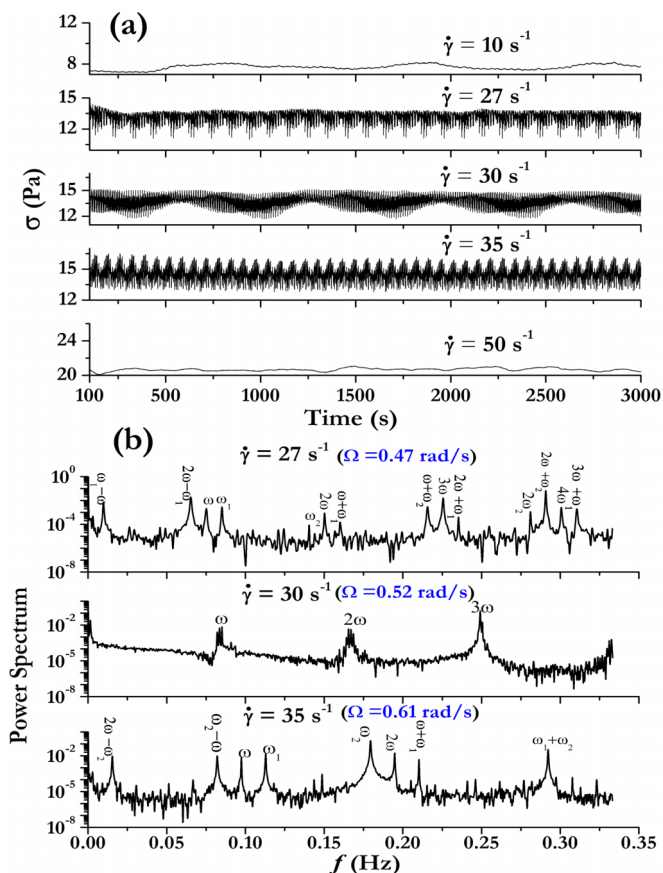
FIG. 8. (a) Stress dynamics in the near-plateau regime at $T = 95\,^\circ$C. The stress oscillation time series at different shear rates. $\dot{\gamma} = 27, 30, 35$ s^{-1} lies within the stress near plateau. $\dot{\gamma} = 10$ and 50 s^{-1} lies below and above the stress plateau, respectively [see Fig. 2(a)]. (b) Corresponding Fourier power spectrum. A few harmonics of the fundamental frequency ω ($= 2\pi f$) are labeled. The fundamental frequencies ω for the shear rates $27, 30, 35$ s^{-1} are 0.47, 0.53, and 0.61 rad/s, respectively. Shearing frequencies calculated using $\Omega = \dot{\gamma}\tan(\alpha)$ are shown within brackets next to the shear rates.

$(\omega, \omega_1, \omega_2)$, there are linear combination of frequencies such as $\omega + \omega_1$, $\omega_1 + \omega_2$, $\omega_2 - 2\omega_1$, and $\omega - \omega_2$. We also performed experiments at a few higher temperatures and overall the stress response was quasiperiodic.

Theoretically dynamics of shared nematogenic fluids considering the coupling of the order parameter to flow have been studied based on the relaxation equation for the alignment tensor [41–44]. It was shown that in the absence of flow alignment the dynamic responses are due to the spatiotemporal fluctuations of the stress [41]. Also a variety of symmetry breaking transient states with out-of-plane director configuration showing complicated periodic or regular chaotic states have been predicted [45]. Recently nematic hydrodynamic incorporating spatial inhomogeneity under controlled shear rate and shear stress has been studied numerically [42]. For a certain range of tumbling parameters the model predicts three distinct states or phases, namely periodic, spatiotemporally chaotic, and aligned. In the N$_{TB}$ phase, we observe some of the features of the stress dynamics predicted in the above references. The similarities of our experimental results with those of the theories are exciting and it encourages for

further experimental work using rheo-optical and rheo-x-ray scattering techniques.

IV. CONCLUSION

In conclusion we have studied the effect of steady shear on the dynamics of a twist-bend nematic liquid crystal. We observe three dynamic regimes in the $\dot{\gamma}$-T diagram. The N$_{TB}$ liquid crystal shows a continuous transition from region I to region II and a discontinuous transition from region II to region III with a finite stress jump. With increasing temperature, the stress jump decreases and the transition is not detectable beyond a particular temperature. The stress is nearly plateaued in region II. The flow behavior in region I and region II is nonlinear with characteristic exponents. However, in region III the flow behavior is linear. The overall flow behavior in region I and region III is similar to that of the SmA phase of 8CB LCs. Thus, under shear, the pseudolayers of N$_{TB}$ behave like a usual SmA layers. In the near-plateau region we have observed both regular periodic and quasiperiodic stress oscillations which are somewhat similar to those were reported in wormlike micellar systems. It appears that with increasing temperature our system moves from regular periodic to quasiperiodic state. Our experiments show some striking similarities with the dynamic stress response of nematogenic fluids predicted recently. Our study unveils the flow dynamics of twist-bend nematic liquid crystals which are promising for further experimental and theoretical studies.

ACKNOWLEDGMENTS

APPENDIX A

Figure 9 shows the variation of stress σ with shear rate $\dot{\gamma}$ in the linear scale. Different regimes described in the main text are marked.
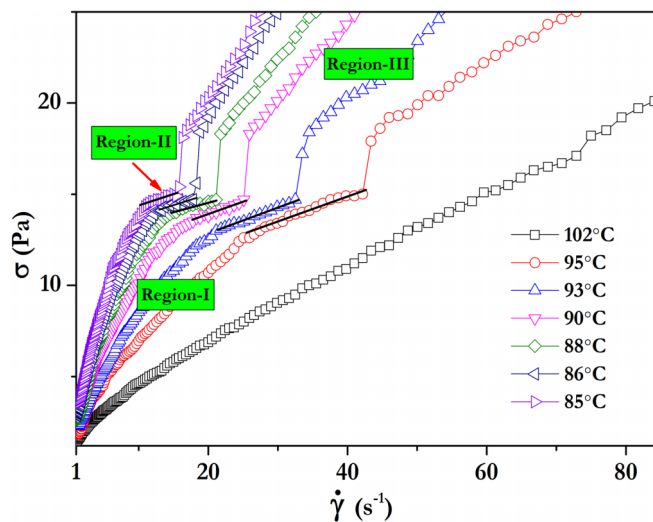
FIG. 9. Shear-rate dependent shear-stress in linear scale from $\dot{\gamma} = 1$ s^{-1} to 85 s^{-1} at different temperatures in the N$_{TB}$ phase.
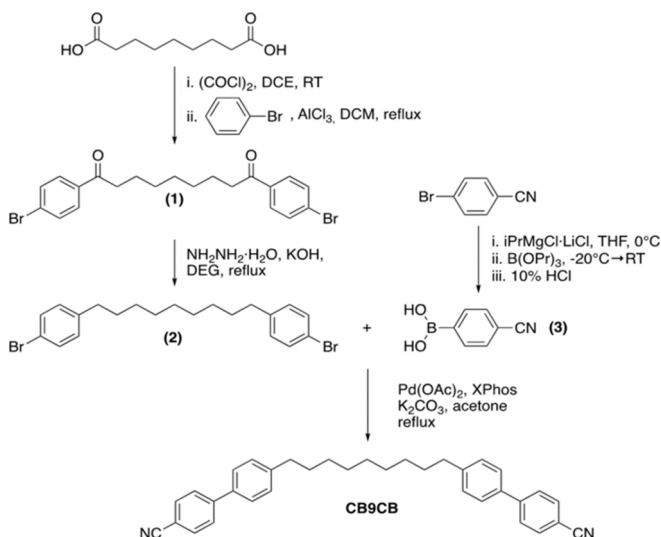
FIG. 10. Synthetic root of the compound CB9CB.

APPENDIX B

The synthesis of CB9CB was performed as described in Fig. 10. Flexible spacer was introduced to the molecule in two steps. In the first step, Friedel-Crafts acylation of bromobenzene with azelaoyl chloride was performed and symmetrical diketone (1) was obtained. Semi-product (1) was then converted to corresponding α, ω-substituted nonane (2) via Wolff-Kishner reduction of diketone. Conversion of the 4-bromobenzonitrile to the (4-cyanophenyl)boronic acid (3) was optimized for magnesium-bromine exchange using lithium chloride complex of isopropylmagnesium chloride solution in THF, so called Turbo-Grignard reagent. The optimal temperature of the Mg-Br exchange was found to be within 0 and 10 °C. In the final step, CB9CB was obtained via Suzuki-Miyaura cross-coupling reaction between reagents (2) and (3) using palladium acetate and XPhos as the catalytic system. Final product was purified by double recrystallization and column chromatography.

Synthesis:

1,9-bis(4-bromophenyl)nonane-1,9-dione (1):

(i) To a stirred solution of azelaic acid (37.6 g; 0.2 mol) in 1,2-dichloroethane (1 dm³) oxalic chloride (36.7 cm³; 0.42 mol) was added with a catalytic amount of N,N-dimethylformamide. The solution was stirred at room temperature for one day until full consumption of azelaic acid. The excess of oxalic chloride and 1,2-dichloroethane were removed under reduced pressure. Crude azelaoyl chloride was taken to the Friedel-Crafts acylation.

(ii) To a stirred solution of AlCl₃ (52.13 g; 0.39 mol) in DCM (500 cm³) azelaoyl chloride was added dropwise. During addition, the temperature went up by 5 °C. The mixture was stirred for two hours until full consumption of aluminium trichloride. Bromobenzene (62.8 g; 0.4 mol) was then added dropwise. The solution was refluxed for 16 hours. The re-

action mixture was then poured out on ice water. Layers were separated, the organic layer was washed four times with water, dried over MgSO4, and concentrated under vacuum. The residue was recrystallized from acetone to yield 50 g (0.1073 mol, 54%) of product 1. m.p. = 131 °C MS(EI) m/z: 446, 385, 267, 198, 183, 155.

1,9-bis(4-bromophenyl)nonane (2):

The solution of 1,9-bis(4-bromophenyl)nonane-1,9-dione (42.8 g; 0.092 mol) and 80% hydrazine hydrate (22.96 g; 0.367 mol) in diethylene glycol (250 cm³) was stirred at 130 °C for one hour. The mixture was cooled down to 120 °C, KOH (29.8 g; 0.533 mol) was added, and the mixture was stirred at 130 °C for two hours. Volatile compounds were then removed, and the mixture was kept at 200 °C for one hour. After cooling to the room temperature, the residue was washed three times with water to remove DEG and dissolved in dichloromethane. The organic layer was then washed three times with water, acidified with 10% HCl and washed five times with water. The organic layer was dried and filtered through silica gel. DCM was evaporated and residue was recrystallized from anhydrous ethanol and acetone.

Obtained crystals were dissolved in hexane, filtered through silica gel and hexane was evaporated. The residue was recrystallized from ethanol and acetone to yield 26.6 g (0.0607 mol; 66%) of product 2. m.p. = 30 °C MS(EI) m/z: 438, 247, 169, 91.

(4-cyanophenyl)boronic acid (3):

The reaction was carried out under N₂ atmosphere. To a stirred mixture of 4-bromobenzonitrile (13.65 g; 0.075 mol) in THF iPrMgCl*LiCl (73 cm³ of 1.04 M solution; 0.075 mol) was added dropwise at 0 °C. The reaction mixture was then stirred at 0 °C for two hours. After cooling to −20 °C, tripropyl borate (15.96 g; 0.085 mol) was added dropwise and the reaction mixture was allowed to reach room temperature. After hydrolysis (with 10% HCl at pH=3) organic solvents were evaporated and crude product was recrystallized twice from water to yield 9.1 g (0.0619 mol; 83%) of product 3. MS(EI) m/z: 187, 157, 129 (mass spectrum of the derived boronic ester with propan-1,3-diol).

α, ω-bis(4,4′-cyanobiphenyl) nonane CB9CB:

The reaction was carried out under N₂ atmosphere. The solution of 1,9-bis(4-bromophenyl)nonane (10 g; 0.02283 mol), (4-cyanophenyl)boronic acid (6.3 g; 0.04556 mol), and potassium carbonate (18.9 g; 0.137 mol) in 160ml of acetone/water mixture (1:1 v/v) was refluxed for 0.5 h. Then Pd(OAc)2 and XPhos (Pd 0.5 mol% and 1 mol% of the ligand) were added, and the reaction was refluxed for two hours. The reaction mixture was poured into water, and the residue was filtered off. The crude product was recrystallized from ethanol and acetone. Obtained crystals were dissolved in DCM, filtered through silica gel, and DCM was evaporated. The residue was recrystallized from ethanol and acetone to yield 10 g (0.0207 mol; 91%) of CB9CB. MS(EI) m/z: 482, 207, 192, 165.

[1] R. G. Larson, *The Structure and Rheology of Complex Fluids* (Oxford University Press, New York, 1999).

[2] T. Divoux, M. A. Fardin, S. Manneville, and S. Lerouge, Annu. Rev. Fluid Mech. **48**, 81 (2016).

[3] J. M. Krishnan, A. P. Deshpande, and P. B. Sunil Kumar, *Rheology of Complex Fluids* (Springer, New York, Dordrecht, Heidelberg, London, 2010).

[4] S. M. Fielding, Soft Matter **3**, 1262 (2007).

[5] P. G. de Gennes, *The Physics of Liquid Crystals* (Oxford University Press, Oxford, 1974).

[6] S. Chandrasekhar, *Liquid Crystals* (Cambridge University Press, Cambridge, 1992).

[7] L. M. Blinov and V. G. Chigrinov, *Electrooptic Effects in Liquid Crystal Materials* (Springer-Verlag, Berlin, 1994).

[8] C. R. Safinya, E. B. Sirota, and R. J. Plano, Phys. Rev. Lett. **66**, 1986 (1991).

[9] O. Henrich, K. Stratford, D. Marenduzzo, P. V. Coveney, and M. E. Cates, Soft Matter **12**, 3817 (2012).

[10] J. Ananthaiah, R. Sahoo, M. V. Rasna, and S. Dhara, Phys. Rev. E **89**, 022510 (2014).

[11] K. Negita, M. Inoue, and S. Kondo, Phys. Rev. E **74**, 051708 (2006).

[12] M. R. Alcantara and J. Vanin, Colloids Surf. A **97**, 151 (1995).

[13] R. Mezzenga, C. Meyer, C. Servais, A. I. Romoscanu, L. Sagalowicz, and R. C. Hayward, Langmuir **21**, 3322 (2005).

[14] W. H. Han and A. D. Rey, J. Rheol. **39**, 301 (1995).

[15] I. Dozov, Europhys. Lett. **56**, 247 (2001).

[16] V. P. Panov, M. Nagaraj, J. K. Vij, Yu. P. Panarin, A. Kohlmeier, M. G. Tamba, R. A. Lewis, and G. H. Mehl, Phys. Rev. Lett. **105**, 167801 (2010).

[17] V. Borshch, Y.-K. Kim, J. Xiang, M. Gao, A. Jkli, V. P. Panov, J. K. Vij, C. T. Imrie, M. G. Tamba, G. H. Mehl, and O. D. Lavrentovich, Nat. Commun. **4**, 2635 (2013).

[18] M. Copic, Proc. Natl. Acad. Sci. USA **110**, 15931 (2013).

[19] D. Chen, J. H. Porada, J. B. Hooper, A. Klittnick, Y. Shena, M. R. Tuchbanda, E. Korblova, D. Bedrov, D. M. Walba, M. A. Glaser, J. E. Maclennana, and N. A. Clark, Proc. Natl. Acad. Sci. USA **110**, 15855 (2013).

[20] C. Meyer, G. R. Luckhurst, and I. Dozov, Phys. Rev. Lett. **111**, 067801 (2013).

[21] Z. Parsouzi, S. M. Shamid, V. Borshch, P. K. Challa, A. R. Baldwin, M. G. Tamba, C. Welch, G. H. Mehl, J. T. Gleeson, A. Jakli, O. D. Lavrentovich, D. W. Allender, J. V. Selinger, and S. Sprunt, Phys. Rev. X **6**, 021041 (2016).

[22] Z. Parsouzi, S. A. Pardaev, C. Welch, Z. Ahmed, G. H. Mehl, A. R. Baldwin, J. T. Gleeson, O. D. Lavrentovich, D. W. Allender, J. V. Selinger, A. Jakli, and S. Sprunt, Phys. Chem. Chem. Phys. **18**, 31645 (2016).

[23] C. Zhu, M. R. Tuchband, A. Young, Min Shuai, A. Scarbrough, D. M. Walba, J. E. Maclennan, C. Wang, A. Hexemer, and N. A. Clark, Phys. Rev. Lett. **116**, 147803 (2016).

[24] C. Meyer and I. Dozov, Soft Matter **12**, 574 (2016).

[25] S. M. Salili, C. Kim, S. Sprunt, J. T. Gleeson, O. Parri, and A. Jakli, RSC Adv. **4**, 57419 (2014).

[26] M. P. Kumar, P. Kula, and S. Dhara, Phys. Rev. Materials **4**, 115601 (2020).

[27] D. A. Paterson, J. P. Abberley, W. TA. Harrison, J. MD Storey, and C. T. Imrie, Liq. Cryst. **44**, 127 (2017).

[28] R. Ganapathy and A. K. Sood, Langmuir, **22**, 11016 (2006).

[29] O. Diat, D. Roux, and F. Nallet, J. Phys. II (France) **3**, 1427 (1993).

[30] D. Roux, F. Nallet, and O. Diat, Europhys Lett. **24**, 53 (1993).

[31] P. Panizza, P. Archambault, and D. Roux, J. Phys. II (France), **5**, 303 (1995).

[32] R. Bandyopadhyay and A. K. Sood, Langmuir **19**, 3121 (2003).

[33] J. Berret, D. C. Roux, and G. Porte, J. Phys. II (France) **4**, 1261 (1994).

[34] J. F. Berret, Langmuir **13**, 2227 (1997).

[35] A. K. Sood and R. Ganapathy, Pramana **67**, 33 (2006).

[36] S. M. Fielding and P. D. Olmsted, Eur. Phys. J. E **11**, 65 (2003).

[37] G. Porte, J.-F. Berret, and J. L. Harden, J. Phys. II (France) **7**, 459 (1997).

[38] R. Bandyopadhyay, G. Basappa, and A. K. Sood, Phys. Rev. Lett. **84**, 2022 (2000).

[39] S. M. Fielding and P. D. Olmsted, Phys. Rev. Lett. **92**, 084502 (2004).

[40] R. Ganapathy and A. K. Sood, Phys. Rev. Lett. **96**, 108301 (2006).

[41] B. Chakrabarti, M. Das, C. Dasgupta, S. Ramaswamy, and A. K. Sood, Phys. Rev. Lett. **92**, 055501 (2004).

[42] R. Mandal, B. Chakrabarti, D. Chakrabarti, and C. Dasgupta, J. Phys.: Condens. Matter **32**, 134002 (2020).

[43] M. Das, B. Chakrabarti, C. Dasgupta, S. Ramaswamy, and A. K. Sood, Phys. Rev. E **71**, 021707 (2005).

[44] D. Chakraborty, C. Dasgupta, and A. K. Sood, Phys. Rev. E **82**, 065301(R) (2010).

[45] G. Rienäcker, M. Kröger, and S. Hess, Phys. Rev. E **66**, 040702(R) (2002).